The Astrophysical Journal Supplement Series, 259:48 (14pp), 2022 April https://doi.org/10.3847/1538-4365/ac5750

Whence the Interstellar Magnetic Field Shaping the Heliosphere?

P. C. Frisch[1], V. Piirola[2], A. B. Berdyugin[2], C. Heiles[3], A. Cole[4], K. Hill[4], A. M. Magalhães[5], S. J. Wiktorowicz[6], J. Bailey[7], D. V. Cotton[8,16,17], L. Kedziora-Chudczer[9], N. A. Schwadron[10], M. Bzowski[11], D. J. McComas[12], E. J. Zirnstein[12], H. O. Funsten[13], C. Harlingten[14], and Seth Redfield[15]
[1] Department of Astronomy and Astrophysics, University of Chicago, Chicago, IL 60637, USA
[2] Department of Physics and Astronomy, University of Turku, FI-20014 Turku, Finland
[3] Department of Astronomy, Campbell Hall, University of California, Berkeley, CA 94720, USA
[4] Greenhill Observatory, School of Natural Sciences, University of Tasmania, Private Bag 37, TAS 7001, Australia
[5] Inst. de Astronomia, Geofisica e Ciências Atmosfericas, Universidade de São Paulo, Brazil
[6] The Aerospace Corporation, El Segundo, CA 90245, USA
[7] School of Physics, UNSW Sydney, NSW 2052, Australia
[8] Monterey Institute for Research in Astronomy, Eighth Street, Marina, CA 93933, USA
[9] University of Southern Queensland, Darling Heights, QLD 4350, Australia
[10] University of New Hampshire, Space Science Center, Morse Hall Rm 407, Durham, NH 03824, USA
[11] Space Research Centre PAS (CBK PAN), Warsaw, Poland
[12] Department of Astrophysical Sciences, Princeton University, Princeton, NJ 08544, USA
[13] Los Alamos National Laboratory, Intelligence and Space Research Division, P.O. Box 1663, Los Alamos, NM 87545, USA
[14] Caisey Harlingten Observatory, Norfolk, UK
[15] Astronomy Department and Van Vleck Observatory, Wesleyan University, Middletown, CT 06459, USA
Received 2021 March 31; revised 2022 January 21; accepted 2022 February 20; published 2022 March 25

Abstract

Measurements of starlight polarized by aligned interstellar dust grains are used to probe the relation between the orientation of the ambient interstellar magnetic field (ISMF) and the ISMF traced by the ribbons of energetic neutral atoms discovered by the Interstellar Boundary Explorer spacecraft. We utilize polarization data, many acquired specifically for this study, to trace the configuration of the ISMF within 40 pc. A statistical analysis yields a best-fit ISMF orientation, $B_{\rm magpol}$, aligned with Galactic coordinates $\ell = 42°, b = 49°$. Further analysis shows the ISMF is more orderly for "downfield" stars located over 90° from $B_{\rm magpol}$. The data subset of downfield stars yields an orientation for the nearby ISMF at ecliptic coordinates λ, $\beta \approx 219° \pm 15°$, $43° \pm 9°$ (Galactic coordinates l, $b \approx 40°$, 56°, $\pm 17°$). This best-fit ISMF orientation from polarization data is close to the field direction obtained from ribbon models. This agreement suggests that the ISMF shaping the heliosphere belongs to an extended ordered magnetic field. Extended filamentary structures are found throughout the sky. A previously discovered filament traversing the heliosphere nose region, "Filament A," extends over 300° of the sky, and crosses the upwind direction of interstellar dust flowing into the heliosphere. Filament A overlaps the locations of the Voyager kilohertz emissions, three quasar intraday variables, cosmic microwave background (CMB) components, and the inflow direction of interstellar grains sampled by Ulysses and Galileo. These features are likely located in the upstream outer heliosheath where ISMF drapes over the heliosphere, suggesting Filament A coincides with a dusty magnetized plasma. A filament 55° long is aligned with a possible shock interface between local interstellar clouds. A dark spot in the CMB is seen within 5° of the filament and within 10° of the downfield ISMF direction. Two large magnetic arcs are centered on the directions of the heliotail. The overlap between CMB components and the aligned dust grains forming Filament A indicates the configuration of dust entrained in the ISMF interacting with the heliosphere provides a measurable foreground to the CMB.

Unified Astronomy Thesaurus concepts: Interstellar magnetic fields (845); Quasars (1319); Interstellar dust (836); Cosmic microwave background radiation (322); Heliopause (707); Plasma astrophysics (1261)

1. Introduction

Magnetic fields pervade interstellar space and modulate the heliosphere configuration. Identifying the past and future heliosphere boundary conditions requires mapping the magnetic field in the surrounding interstellar medium (ISM). Two large-scale magnetic structures extend into the solar vicinity within 100 pc, the interarm magnetic field directed toward ℓ, $b = 80°$, 0° (Heiles 1998) and the evolved nearby Loop I magnetic superbubble with a diameter of over 80° (Mathewson & Ford 1970; Frisch 1996; Wolleben 2007; Santos et al. 2011; Berdyugin et al. 2014; Frisch & Dwarkadas 2018; Panopoulou et al. 2021). Starlight that is linearly polarized by aligned foreground interstellar dust grains (ISDGs) provides a robust diagnostic of the orientation of the interstellar magnetic field (ISMF) for diverse interstellar environments. Polarization measurements from the 20th century identified an ISMF within 30–40 parsecs of the Sun (Mathewson & Ford 1970; Piirola 1977; Tinbergen 1982; Leroy 1993). Recent high-sensitivity measurements display nearby interstellar magnetic filaments, including filaments that echo geometries of the

[16] Western Sydney University, Locked Bag 1797, Penrith-South DC, NSW 1797, Australia.
[17] University of Southern Queensland, Centre for Astrophysics, Toowoomba, QLD 4350, Australia.

heliosheath (Frisch et al. 2015b, 2018) and the local interstellar ISMF (Piirola et al. 2020). Interstellar polarization strengths increase steadily with distance along the eastern rim of Loop I (Bailey et al. 2010; Santos et al. 2011). The Loop I geometry (Wolleben 2007) and flow of local interstellar gas through the local standard of rest (LSR; Frisch et al. 2002; Frisch & Schwadron 2014) are consistent with an origin for the surrounding interstellar gas as an outflow from the nearest regions of the Loop I superbubble.

The large fraction of refractory elements in the gas phase of the local interstellar medium (LISM) indicates that local ISDGs were eroded by interstellar shocks (Frisch et al. 1999, 2011, abbreviated as F99 and FSR11, respectively). Grain erosion yields smaller grains that increase extinction at shorter wavelengths and shift polarization peaks blueward. Indications of relatively blue interstellar polarizations were first measured for nearby stars by Marshall et al. (2016). Cotton et al. (2019) found that stars within the Local Hot Bubble have a bluer peak polarization than those beyond it. Subsequent studies focusing on the very nearby stars α Oph and HD 172555 found bluer polarization colors than typical (Marshall et al. 2020; Bailey et al. 2021).

The organization of interstellar gas in the LISM is not fully understood. Kinematical models assume that the interstellar gas velocities trace physically distinct clouds (Redfield & Linsky 2008, RL08), or alternatively a kinematically disturbed flow of shocked interstellar gas (Gry & Jenkins 2014). Simulations of the ionization of the Local Interstellar Cloud (LIC) supplying interstellar gas to the heliosphere (Slavin & Frisch 2008; Frisch et al. 2011) show the Sun is embedded in a partially ionized gas that will couple to the ISMF. LIC models based on an ISMF configuration include assumptions that the ISMF is parallel to the LIC cloud surface (Frisch 1994) and that a magnetized interstellar shock is within a few parsecs (Grzedzielski & Lallement 1996).

Measurements by the Interstellar Boundary Explorer (IBEX)-Lo have yielded data on the interaction of interstellar He and the heliosphere and confirmed that the ISM around the heliosphere is partially ionized (Fuselier et al. 2009; Möbius et al. 2009; Swaczyna et al. 2015). Analysis of the inflow of interstellar neutral He at 1 au gives an upwind direction toward ecliptic coordinates $\lambda = 255.^{\circ}8 \pm 0.^{\circ}5$, $\beta = 5.^{\circ}16 \pm 0.^{\circ}10$, velocity $= 25.8 \pm 0.4$ km s^{-1}, and a cloud temperature 7439 ± 260 K (Bzowski et al. 2015). Comparison with the first measurement of the velocity of interstellar H° inside of the heliosphere (-24.1 ± 2.6 km s^{-1}; Adams & Frisch 1977), indicates the flow velocity of interstellar H° through the heliosphere has been relatively steady for the past ~45 yr. A fundamental symmetry of the heliosphere is the *B–V* plane, formed by the directions of the ISMF ($\boldsymbol{B}_{is}$) and the interstellar velocities of inflowing neutral particles ($\boldsymbol{V}_{is}$); see Appendix A.

An unexpected probe of the very local ISMF appeared with the discovery of a "ribbon" of energetic neutral atoms (ENAs) generated by the interaction between the ISMF and the heliosphere (McComas et al. 2009; Schwadron et al. 2009). The ribbon appears where the magnetic field in the partially ionized surrounding interstellar gas drapes over the heliosphere and becomes quasi-perpendicular to sightlines. The ribbon ENAs first detected by IBEX-Hi (Funsten et al. 2009) are due to secondary ENA formation upstream of the heliosphere. Secondary ENAs arise by charge exchange with 1 keV protons trapped in small gyroradii around the field lines of the ISMF draped over the heliosphere (Heerikhuisen et al. 2010).

Table 1
Magnetic Field Orientations in Galactic and Ecliptic Coordinates

Description	Galactic Coordinates	Ecliptic Coordinates	References
Simulation	ℓ, $b = 26.^{\circ}0 \pm 0.^{\circ}78$, $50.^{\circ}1 \pm 0.^{\circ}61$	$\lambda = 227.^{\circ}28 \pm 0.^{\circ}69$, $\beta = 34.^{\circ}62 \pm 0.^{\circ}45$	Z16
$B_{\rm magpol}$	$(l, b) = (42°, 49°)$	$(\lambda, \beta) = (229°, 45°)$	Section 3
$B_{\rm magpol} < 0$	$(\ell, b) = 40°$, $56°$ ($\pm 17°$).	$(\lambda, \beta) = (219° \pm 15°$, $43° \pm 9°)$	Section 3

Note. The weighted mean field strength is 2.93 ± 0.08 μG.

The relation between the ribbon, the ISMF, and the orientation of the *B–V* plane in space was also demonstrated indirectly by in situ sampling of interstellar neutral atoms by IBEX-Lo. The presence of a significant ISMF (>3 μG) deforms the heliosphere from axial symmetry. Ribbon ENAs appear as an arc selected by angle and energy, analogous to the optical dispersion in a rainbow. Models placing the IBEX ribbon in regions where outflowing plasma is spatially retained by Alfvén waves beyond the heliopause also yield predictions of interstellar Alfvén speeds averaging 42.7 ± 3.0 km s^{-1} (Schwadron & McComas 2021).

A global MHD-kinetic model of the heliosphere (Pogorelov et al. 2008) was utilized by Zirnstein et al. (2016, Z16) to relate the directions of the ISMF field perturbed by the heliosphere to the unperturbed ISMF in the ISM. Modeling of the energy-dependent IBEX ribbon determines the magnetic field directions beyond the influence of the heliosphere (see Table 1). The weighted mean field strength is 2.93 ± 0.08 μG over all energies.

This paper is organized as follows. We use the largest sample of local polarization data to date (Section 2) for evaluating the local ISMF. These data sample starlight that is linearly polarized by interstellar material with low column densities typical of the intercloud medium where $N(\mathrm{H}^{\circ}) < 10^{18.5}$ cm^{-2} (Bohlin et al. 1978; Frisch et al. 2011). The majority of the data have been collected during the 21st century during solar cycle 24, 2008 December through 2019 December (Piirola et al. 2020). Section 2 summarizes the 20th and 21st century polarization data used in this study, where over half of the 21st century data are measurements by Piirola et al. (2020).

The best-fitting ISMF direction to the ensemble of data is determined using a least-squares analysis of polarization position angle data applied to the whole sky as well as the upfield and downfield hemispheres (Section 3). Section 4 describes a shock-like feature in the downfield polarization data (Section 4.1) that borders a cosmic microwave background (CMB) dark spot (Section 4.2). A discussion of new results is presented in Section 5. The best-fitting ISMF orientation agrees with the direction derived from IBEX ribbon models (Section 5.1). Magnetic structures are seen throughout the sky (Section 5.2), including filaments (Section 5.2.1) and arcs (Section 5.2.2). Some polarizations echo geometries of the outer heliosheath (Section 5.3), including the Voyager 3 kHz data (Section 5.3.1), compact QSO scintillation sources (Section 5.3.2), a symmetry with respect to CMB multiple moments (Section 5.3.3), and the IBEX ribbon (Section 5.3.4). A summary of results is given in Section 6. Appendices present supplementary discussions of the heliosphere and *B–V* plane

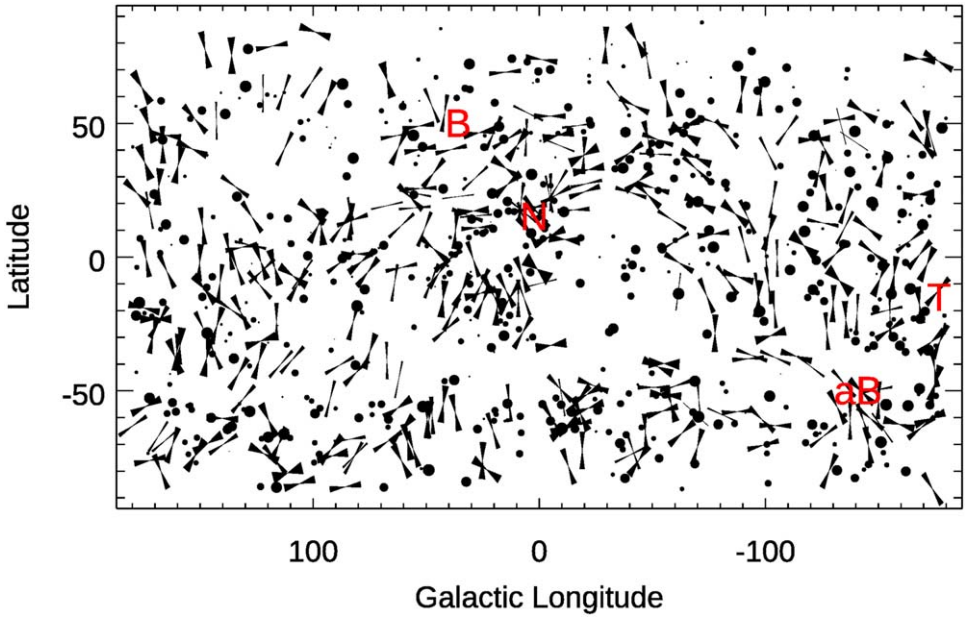

Figure 1. Polarization position angles are shown with fan-shaped symbols for data where $P/\Delta P > 1.95$, and with dots where $P/\Delta P < 1.95$. Angular widths of the fan-shaped symbols show twice the measurement uncertainties of polarization position angles. Dot sizes are proportional to $P/\Delta P$. The symbols "B," "aB," "N," and "T" give the directions of the IBEX ribbon ISMF direction, 180° from that location, and the heliosphere nose and tail directions, respectively.

(Appendix A), intrinsic stellar polarizations (Appendix B), and a listing of stars assigned to Filament A (Appendix C).

2. Polarization Data

Polarization position angle data provide the basis for evaluating the best-fit ISMF direction to the ensemble of polarization data. The polarization position angle is defined as the angle between the orientation of the linear polarization and the north pole of the coordinate system, where positive position angles increase to the east. Models in which charged spinning grains align with the most optically opaque axis perpendicular to the magnetic field lead to polarization position angles parallel to the ISMF (Andersson et al. 2015; Lazarian & Hoang 2019).

2.1. Data

Identifying the ISMF that shapes the heliosphere in starlight polarization data involves sampling interstellar polarizations of stars in a volume of space large enough to yield good sampling of the local ISMF, but small enough to exclude distant ISMF components less likely to extend to the heliosphere. Stars utilized in this study are within 40 pc according to the Hipparcos catalog. This limit includes stars inside the Local Bubble and outside the nonlocal high-column-density regions of Loop I.

The data set includes measurements of the linear polarizations of over 800 stars within 40 pc of the Sun, 331 of which have measurable polarizations and are used in the current numerical analysis (Figure 1). Of this sample 60% of the stars have $P/\Delta P < 1.95$, and 40% have $P/\Delta P > 1.95$, where P and ΔP are the polarization strengths and uncertainties. The plot limit $P/\Delta P = 1.95$ is somewhat arbitrary and was selected to allow good spatial coverage of the displayed data.

Data collected during the 20th and 21st centuries represent 46% and 54% of the data set, respectively. The data collected during the 20th century are from Piirola (1977), Tinbergen (1982), Leroy (1993), and Heiles (2000).[18] The data collected in the 21st century include measurements acquired for this survey with the Dipol-2 polarimeter mounted at the UH88, T60, and H127 telescopes (Piirola et al. 2020), data acquired at the Pico dos Dias Observatory of the Laboratório Nacional de Astrofísica in Brazil, at the remotely controlled 60 cm KVA telescope and 2.52 m Nordic Optical Telescope, both located at Observatory of Roque de los Muchachos, La Palma, Canary Islands, Spain, at Lick observatories (F15a, F15b; Wiktorowicz & Nofi 2015), and data acquired with the HIPPI instrument primarily at the Anglo-Australian Telescope observatory (Bailey et al. 2015, 2017; Cotton et al. 2016, 2017; Marshall et al. 2016). Additional data on the polarizations of nearby stars acquired during the 21st century are provided by the Bailey et al. (2010) and Santos et al. (2011) studies. About half of the data used in this study were collected by Piirola and collaborators for the purpose of mapping the ISMF in the heliosphere environment.

Polarization data are displayed in Galactic coordinates in Figure 1 and in Galactic, ecliptic, and celestial coordinates in Figure 2.[19] Polarization position angles are displayed for stars where $P/\Delta P \geqslant 1.95$. The central axis of "fan-shaped" symbols indicates polarization position angles in the specified coordinate system; the full angular width of the fan symbol represents twice the position angle uncertainty. Data for stars where $P/\Delta P < 1.95$ are plotted using dots that have diameters linearly proportional to $P/\Delta P$. Regions where measurements are restricted to polarizations represented with small dots have multiple possible explanations, such as a dust deficit, inefficient grain alignment, magnetic fields parallel to the sightline, or a foreground depolarization screen.

[18] The Tinbergen (1982) data were obtained in 1973 (J. Tinbergen, private communication).

[19] Position angles are converted between equatorial, Galactic, and ecliptic coordinates based on the conversion formula provided in a footnote in Appenzeller (1968).

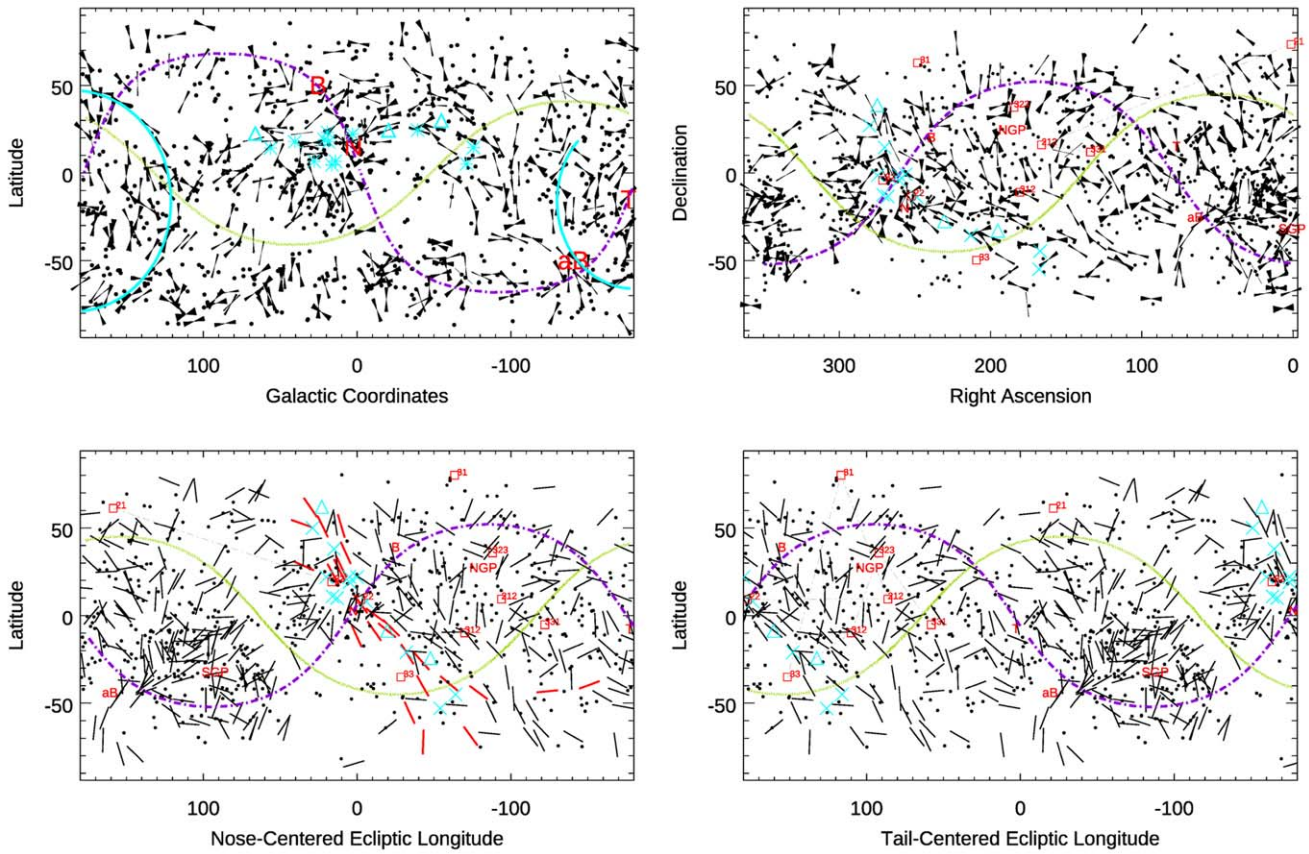

Figure 2. Polarization position angles are mapped in Galactic (top left), celestial (top right), and nose-centered and tail-centered ecliptic coordinates (bottom left and bottom right). Cyan triangles indicate sightlines toward three compact QSOs aligned with Filament A (Section 5.3.2). Cyan "X" marks show Voyager 3 kHz emissions (Section 5.3.1). The two large cyan-colored circular arcs (upper left) are sections of circles centered at $\ell, b = 184°, -16°$ ("Arc 1": $\lambda, \beta = 74.^{\circ}9, -5.^{\circ}9$, radius 63°) and $\ell, b = 180°, -16°$ ("Arc 2": $\lambda, \beta = 73.^{\circ}0, -2.^{\circ}5$, radius 50°) The green line separates the hemispheres defined by $B_{\rm magpol} < 0$ and $B_{\rm magpol} > 0$, where $B_{\rm magpol}$ represents the best-fitting ISMF orientation $\ell, b = 42°, 49°$ (Section 3). The B–V plane is plotted with a purple dashed–dotted line.

Figure 1 also displays heliosphere "spacemarks" (representing notable features in space; see Appendix A). The heliosphere nose and tail directions are defined by the direction of primary interstellar He° atoms flowing into the heliosphere (Schwadron et al. 2015a; Bzowski et al. 2019) and the direction of the ISMF shaping the heliosphere (Funsten et al. 2013; Schwadron et al. 2015b, Z16).

Stellar distances are based on astrometric data in the Hipparcos catalog (Perryman 1997; Van Leeuwen 2008). Distance uncertainties are calculated based on the distance that divides the distance uncertainty cones created by parallax uncertainties into equal volumes (Hanson et al. 2003; Frisch et al. 2015b). The astrometric (derived from stellar spectral types) and parallax distances generally match. The study in this paper utilizes stars where the distance uncertainty interval includes a distance of 41 pc or less. The full range of distance uncertainties for data used in this analysis extends to a maximum possible distance of 63 pc for the star HIP 118020.

The data used for this study do not represent a randomly selected sample of nearby stars. Over half of the stars were acquired for this project to map the very local ISMF. Stars selected for new measurements were sometimes biased by positive detections of polarizations in adjacent regions. If two adjacent stars show aligned polarization position angles, further observations might select target stars to test whether an extended magnetic feature is present. With the current data set it is not feasible to evaluate the possible effect of the target star selection on the detected magnetic structure.

The measurement uncertainties for the polarization data differ among the underlying data sets since polarimeter sensitivities have improved over the ∼60 yr interval during which the data incorporated into this study were collected. Stars with intrinsic polarizations may remain in the sample, although efforts have been made to exclude such stars by avoiding active stars, giant stars, stars where photometric and astrometric distances differ, and capping $P/\Delta P$ at 6.0 to minimize possible biases due to unidentified active stars (Appendix B). Data collected since 2000 tend to be more accurate than data collected earlier, and also are likely to sample lower-column-density ISM than 20th century data. This study does not utilize absolute polarization strengths; however, differences in instrumental sensitivities will affect the measurement uncertainties that enter into the fitting process (Section 3).

Magnetic field orientations are reconstructed from these data by assuming that the linear polarization is parallel to the ISMF and the most opaque dust grain axis is oriented perpendicular to the ISMF. The stars average one star per 7 square degrees of the sky but are unevenly distributed, with gaps in the spatial coverage (Figure 1). Spatial gaps between measurements might be due to star clustering or to opaque foreground interstellar or heliospheric material. The all-sky coverage of these data enables the ISMF direction to be determined over both large

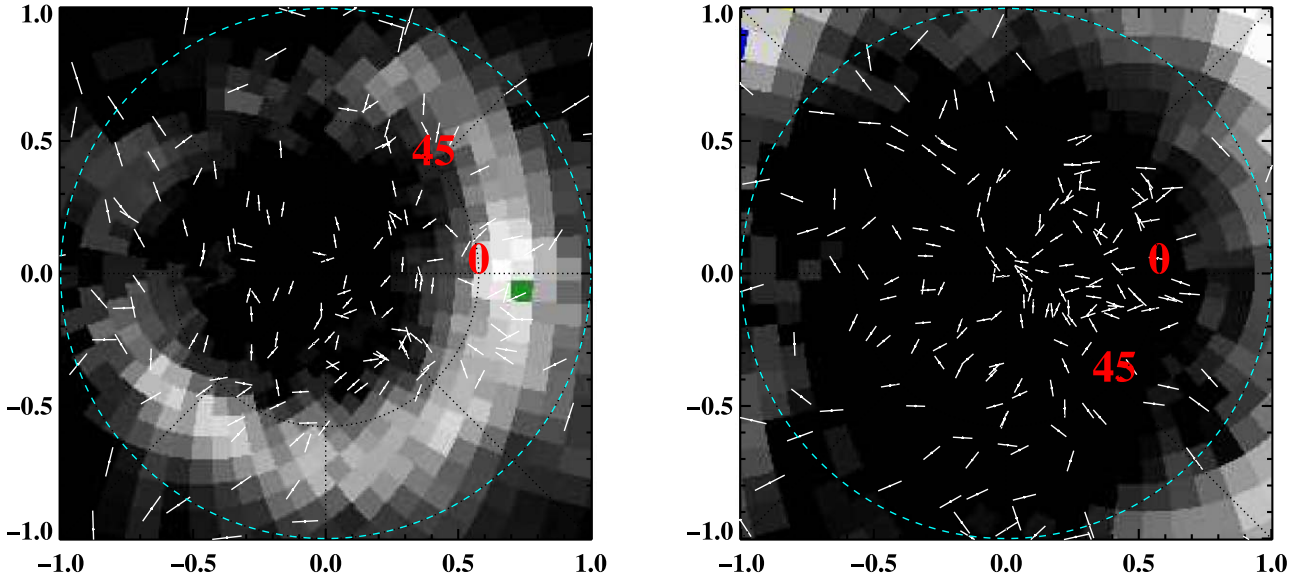

Figure 3. Stereographic projections of polarization position angles are shown for a coordinate system centered on poles located at the best-fitting ISMF to all data, ℓ, $b = 42°$, 49°, and 180° away. Stars above/below the equator of the projection (the cyan dashed line) are shown in the left/right panels. Labels "45" and "0" denote the $\ell = 45°$, and $\ell = 0°$ locations in the plane of the projections. The semicircular band of shaded squares displays the 1.7 keV IBEX ribbon from Year 1 of the IBEX mission. The green "N" marks the heliosphere nose direction.

scale and the small angular scales corresponding to the interstellar counterpart of the ISMF shaping the heliosphere.

2.2. Alternative Displays of Polarization Data

Figure 2 displays polarization data in Galactic, ecliptic, and celestial coordinates, along with features of the outer heliosheath. The ISMF within 40 pc screens data tracing a wide range of astrophysical phenomena, such as the configuration of nearby partially ionized interstellar clouds (commonly shown in Galactic coordinates), Galactic cosmic ray fluxes (often displayed in celestial coordinates), and heliosphere data. The angle between the solar equator and the ecliptic plane is 7°.25. We follow the convention of displaying data in ecliptic coordinates rather than heliographic coordinates. Figure 2 also displays notable heliosphere "spacemarks," the directions of the heliosphere nose and tail, the ISMF direction, the *B–V* plane (Appendix A), the plane separating $B_{\rm magpol} > 0$ and $B_{\rm magpol} < 0$ stars (Section 3), locations of Voyager kilohertz emissions observed in the 20th century (Section 5.3.1), local QSO compact scintillation sources (Section 5.3.2), large magnetic arcs around the heliotail (Section 5.2.2), and CMB components that overlap Filament A (Section 5.3.3).

Figure 3 displays the polarization position angles in stereographic projections separated into the hemispheres of "upfield" stars (left, $B_{\rm magpol} > 0$) and "downfield stars" (right, $B_{\rm magpol} < 0$), defined with respect to the best-fitting ISMF found from the full set of data (Section 3). Figure 3 also displays the location of the IBEX ribbon at 1.1 keV, based on Year 1 data. Stereographic projections display the true angular orientation for polarization position angles. Polarization position angles that are perpendicular to the IBEX ribbon in Figure 3 are parallel to the ISMF, as expected.

3. Magnetic Field Orientation Traced by Polarization Data

We examine the structure of the local ISMF by applying a χ^2 fit to the orientations of the polarization position angles (Section 2). Our model is that the polarization position angle for every star n (PA_n) is aligned with the local magnetic pole at Galactic coordinates ($l_{\rm magpol}$, $b_{\rm magpol}$). For this idealized model, the expectation value for the sine of each polarization position angle $\mathrm{PA}_n(l_{\rm magpol}, b_{\rm magpol})$ is zero, so the variance is $\mathrm{var}(\mathrm{PA}_n(l_{\rm magpol}, b_{\rm magpol})) = \sin^2(\mathrm{PA}_n)$. The corresponding reduced χ^2 is

$$\widehat{\chi^2}(l_{\rm magpol}, b_{\rm magpol}) = \frac{1}{M}\sum_n \frac{\sin^2(\mathrm{PA}_n)}{\sigma^2(\mathrm{PA}_n)}, \quad (1)$$

where M is the total number of measurements. $\sigma(\mathrm{PA}_n)$ is the intrinsic uncertainty in the measured PA_n and is given by $0.5\,\sigma(P_n)/P_n$. Both P_n and uncertainty $\sigma(P_n)$ are known from the observed starlight polarizations.

In practice, we use only those stars that have (1) $(P_n/\sigma(P_n)) > 1.95$, (2) we cap $(P_n/\sigma(P_n))$ at 6.0 to avoid unrecognized intrinsic stellar polarizations, and (3) we use only those stars for which the distance uncertainty range includes a distance of less than 41 pc. This provides a sample of 331 stars that are distributed roughly randomly over the celestial sphere.

We use all 331 stars to calculate $\widehat{\chi^2}$ for an all-sky grid of ($l_{\rm magpol}$, $b_{\rm magpol}$). Figure 4, left panel, shows the resulting image of $\widehat{\chi^2}$. By inspection, the minimum occurs at ($l_{\rm magpol}$, $b_{\rm magpol}$) $\approx (42°, 49°)$, at which $\widehat{\chi^2} = 1.54$. This is fairly close to unity, which it should be because $\widehat{\chi^2}$ is the mean of the individual weighted variances for the stars, each of which should be close to unity. For convenience, we normalize the contours in Figure 4 so that the minimum value is unity.

Next, we test the uniformity of the field by splitting the stars into two independent groups: 146 "upfield" stars, located in the hemisphere toward ($l_{\rm magpol}$, $b_{\rm magpol}$) (denoted $b_{\rm magpol} > 0$); and 185 "downfield" stars, located in the opposite hemisphere (denoted $b_{\rm magpol} < 0$). Figure 4, middle and right panels, respectively, show the corresponding $\widehat{\chi^2}$ images. The two stellar groups suggest different directions for the upstream and downstream magnetic poles.

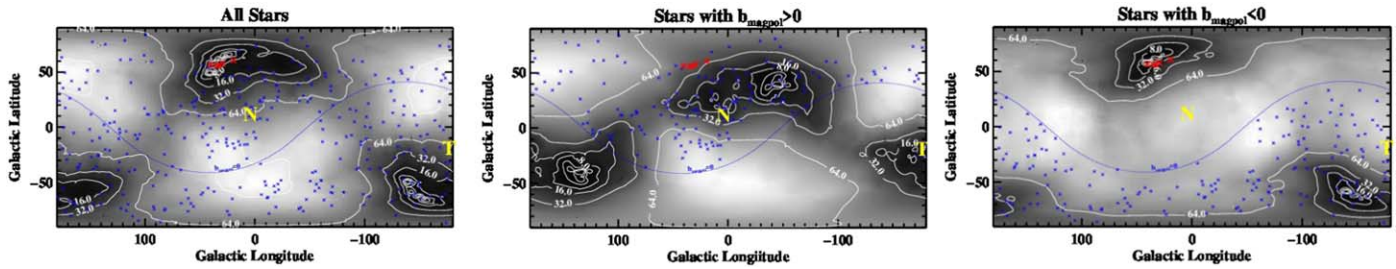

Figure 4. Left panel: all-sky Galactic-coordinate map of the normalized $\widehat{\chi^2}$ for all 331 stars (Section 3). The minimum occurs near $(l, b) = (42°, 49°)$. The middle panel displays the normalized $\widehat{\chi^2}$ for the $b_{\rm magpol} > 0$ (upfield) stars, and the right panel for $b_{\rm magpol} < 0$ (downfield) stars. The line $b_{\rm magpol} = 0$ in all three panels separates the $b_{\rm magpol} > 0$ and $b_{\rm magpol} < 0$ hemispheres. Blue asterisks show the locations of stars used in each analysis. "N" indicates the heliosphere nose. Red "Xs" represent the ISMF directions obtained from ENA ribbon centers measured by IBEX-Hi (Section 3).

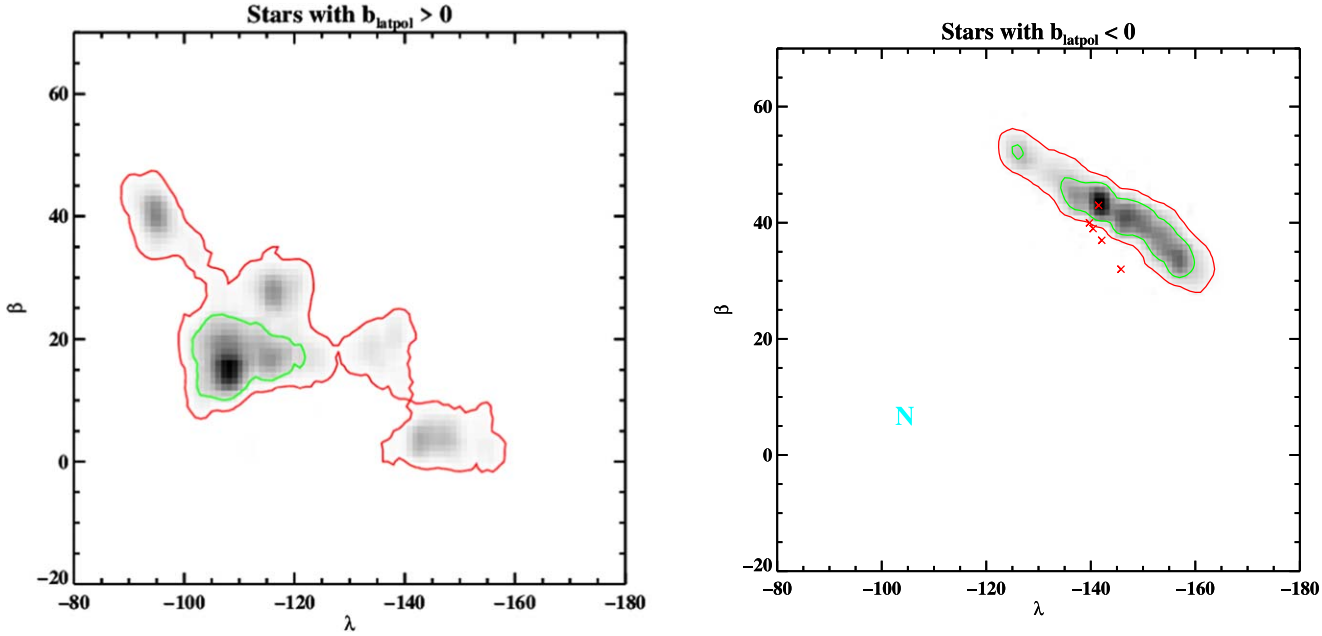

Figure 5. Ecliptic-coordinate maps of the probability density function (Equation (1)) of the location of the magnetic pole for upfield stars (left panel) and downfield stars (right panel). The PDF is represented both by gray scale (increased darkness indicates increased PDF) and two contours. The red contour is the 2σ contour, which envelopes 95.4% of the PDF, and the green contour is the 1σ contour (68.4%). Red X's indicate locations of ribbon centers for the five IBEX energy bands of IBEX at energies 0.7, 1.1, 1.8, 2.7, and 4.3 keV, top to bottom (see text).

We examine the difference between the two groups using the bootstrap technique (Vandeportal et al. 2019, Chapter 4.5). We have a list of $N = 185$ downfield stars, each with its own set of data points, including sky position and polarization position angle. In the bootstrap method, one creates a new list of N stars by randomly selecting stars from the original list. Some of the N original stars will appear twice or more in the new list, and some will not appear at all. One then uses the data points from the stars in the new list to obtain $(l_{\rm magpol}, b_{\rm magpol})$ as we did above. One repeats this for, say, 8000 times, which provides 8000 derived values for $(l_{\rm magpol}, b_{\rm magpol})$. The resulting histogram of 8000 results is a good approximation to the true probability density function (PDF) of $(l_{\rm magpol}, b_{\rm magpol})$.

Figure 5 shows the PDFs for the $B_{\rm magpol} > 0$ (left) and $B_{\rm magpol} < 0$ (right) sets of stars. The PDF is represented both by gray scale, where an increase in darkness indicates larger values for the PDF, and two contours. The red contour is the 2σ contour, which envelopes 95.4% of the PDF, and the green contour is the 1σ contour, enveloping 68.4% of the PDF. The difference between the best-fitting ISMF to these two star samples is clear. The downfield stars, shown in the right panel, trace a more uniform ISMF direction, with much more compact contours, than the upfield stars in the left panel. Moreover, the peaks of the PDFs differ in location by about 40°, which is far more than the uncertainties. The peak of the PDF obtained from downfield stars is located at ecliptic coordinates $(\lambda, \beta) \approx (219° \pm 15°, 43° \pm 9°)$, or $(l, b) \approx (40°, 56°, \pm 17°)$ in Galactic coordinates. This best-fitting ISMF is in agreement with the ISMF shaping the IBEX ribbons determined from the Z16 models (Table 1).

The contours of the PDFs are conspicuously elongated with an orientation that is quasi-parallel to the spatial alignment of the centers of the individual IBEX ribbon energy channels. Figure 5, right, also displays the centers of the IBEX ribbon for the five energy channels of IBEX-Hi, 0.7, 1.1, 1.8, 2.7, and 4.3 keV (Funsten et al. 2013). The good correspondence between the ISMF shaping the heliosphere from ribbon simulations (Z16) and the ISMF derived from the downfield polarization data suggests the heliosphere is currently embedded in a larger-scale ordered ISMF. The ribbon center at 0.7 keV provides the best match to the ISMF obtained from IBEX ribbon models (Z16).

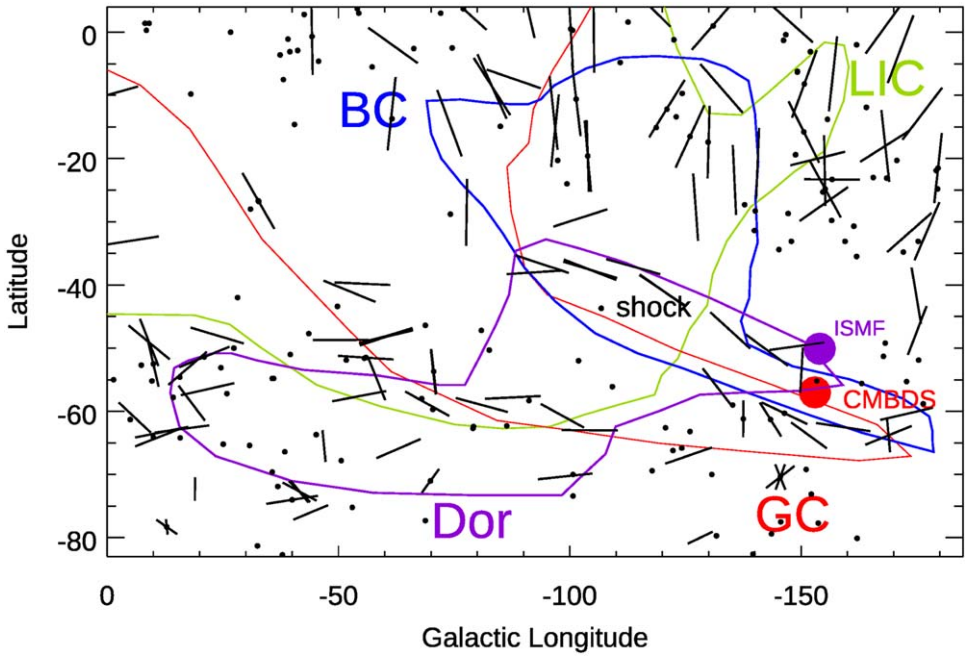

Figure 6. Polarization position angles in the region of a possible shock interface between four local clouds defined by RL08, the cloud around the heliosphere (LIC, green), the Doradus cloud (DOR, purple), the Galactic Center cloud (GC, red) and the Blue Cloud (BC, black). Locations are shown for the downfield interstellar magnetic field (from Z16, large purple dot) and a cosmic microwave background dark spot with radius ∼10°–11° (Section 4).

Table 2
Relative LSR Velocities of Proximate Clouds

Cloud Pair	Angle between LSR Velocities	Relative LSR Velocities (km s^{-1})	Temperatures (K)
Blue/Dor	69°	−39	3900 ± 2300/7000
G/Dor	43°	−27	5500 ± 400/7000
G/Blue	69°	−13	5500 ± 400/3900 ± 2300

4. Downfield Shock and Cosmic Microwave Background Dark Spot

4.1. Downfield Shock

Measurements of UV and extreme-UV interstellar absorption lines toward nearby stars indicate the Sun travels through a region containing warm, low-density partially ionized "inter-cloud" gas with ionizations dominated by photons from ϵ CMa (Rogerson et al. 1973; Bohlin et al. 1978; Lehner et al. 2003, FSR11). Low-density partially ionized gas couples to the ISMF so that the ISMF may influence the spatial configuration of local clouds that are kinematically defined. One region shows evidence of cloud boundaries aligned with the ISMF. A magnetic filament traced by polarization data has been identified within 20 pc (see Figure 5 in Piirola et al. 2020). This filament coincides with the boundaries of four local interstellar clouds in the 15-cloud model of RL08. Three clouds have boundaries that are quasi-parallel and aligned with polarization position angles in the interval $b = -35°$ to $-70°$ and $\ell = 180°$ to 270° (Figure 6). In this region Doradus (DOR, purple), Galactic Center cloud (GC, red) and Blue Cloud (BC, black) have boundaries that are quasi-parallel and aligned with polarization position angles (Figure 6). The boundaries of the LIC cloud (green), nominally around the heliosphere, do not align with this magnetic filament. Velocities of possible collisions between these three clouds are estimated from cloud velocities through the local standard of rest (LSR; Table 2) based on RL08 data and LSR velocities in Frisch & Schwadron (2014).

Interactions between the Blue and DOR clouds would be supersonic and/or super-Alfvénic for cloud properties similar to the cloud around the heliosphere (Table 2) so that a shocked interface may form. A quasi-perpendicular MHD shock between the GC cloud and the LIC has been predicted (Grzedzielski & Lallement 1996). Figure 6 shows the location of the magnetic field that is quasi-parallel to the nearly aligned boundaries of the GC, BC, and DOR clouds, and the polarization position angles tracing the possible shock interface formed from collisions of these three clouds.

Three intraday variable QSOs were postulated by Linsky et al. (2008) to sample dense nearby interstellar plasma regions formed from local colliding clouds. These QSOs are located along the shocked interface (see Figure 2, upper left). The scintillations creating the intraday variability for PKS0405-385 (ℓ, $b = 241.^{\circ}3$, $-47.^{\circ}9$) and PSR J0437-4715 (ℓ, $b = 253.^{\circ}4$, $-47.^{\circ}9$) may arise from a super-Alfvénic shock creating dense plasma pockets aligned with the magnetic field compressed between the colliding clouds.

4.2. Possible Explanations for a Cosmic Microwave Background Dark Spot

A roughly circular "dark spot," with a diameter of ∼10°–11°, is found in the CMB (Schwarz et al. 2016). The dark spot

is located at ℓ, $b = 207°$, $-57°$ so that it overlaps the DOR cloud boundary and also borders the interfaces of the GC and BC clouds (Figure 6). An angle of $179.^{\circ}0 \pm 0.^{\circ}9$ separates the dark spot and the direction of the ISMF shaping the heliosphere found from IBEX ribbon models of Z16.

Polarization position angles of linearly polarized starlight in the diffuse ISM trace the least-opaque axis of the dust grains, parallel to the ISMF. The sightline with largest grain opacities occurs at angles perpendicular to the ISMF (Lazarian & Hoang 2019). This configuration leads to a possible explanation for the dark spot as due to ISDGs trapped on the magnetic field, creating an asymmetric shadow on the CMB when viewed in sightlines parallel to the ISMF.

In sightlines displaying starlight that is linearly polarized in the diffuse ISM, the most transparent axis of the grain is parallel to the ISMF, and the most opaque axis of the grain is perpendicular to the ISMF. In principle a viewpoint parallel to the ISMF will sample larger grain cross sections than will perpendicular sightlines. The parallel viewpoint also samples turbulence that is perpendicular to the ISMF such as generated by Alfvén waves. The angular width of the dark spot, $\sim 10°$, is comparable to interstellar magnetic turbulence identified upstream of the heliosphere nose, where polarization data indicate magnetic turbulence of $9.^{\circ}6$ (Frisch et al. 2015a). These data are consistent with the possibility that magnetic turbulence contributes to the width of the dark spot.

5. Discussion

5.1. Best-fitting Interstellar Magnetic Field to Polarization Data

The ISMF structure traced by the polarization data varies across the sky. The ISMF orientation that provides the best fit to the full data sample ($B_{\rm magpol}$ at ℓ, $b = 42°$, $49°$; Section 3) is used to characterize the organization of the ISMF. The ISMF exhibits more compact probability contours in the magnetic hemisphere containing the downfield $B_{\rm magpol} < 0$ stars, compared to the upfield stars that are within $90°$ of ℓ, $b = 42°$, $49°$ (Section 3, Figure 5). Regions of maximum probability extend between λ, $\beta \approx 215°$, $3°$ and λ, $\beta \approx 270°$, $40°$ for upfield stars. The downfield stars yield a compact PDF peak aligned with ecliptic coordinates $(\lambda, \beta) = (219° \pm 15°, 43° \pm 9°)$.

The 2σ fit contour for downfield stars (Figure 5) shows an increasingly large angular distance from the ENA ribbon centers as the ENA energy increases (Funsten et al. 2013). The energy dependency of the angular separations between the best-fitting ISMF and ribbon centers suggests that the lowest-energy ENAs (the 0.7 keV band) trace the ISMF aligning the grains.

Configurations of several filaments are consistent with aligned ISDGs bound to the ISMF draping over the heliosphere (Section 5.2). Large ISDGs and interstellar gas enter the heliosphere from the same upwind direction to within the 1σ uncertainties (Section 5.2.1). Polarization position angles for stars within $90°$ of $B_{\rm magpol}$ are more likely to trace small grains trapped on the perturbed ISMF draping over the nose of the heliosphere than the downfield stars. The distorted polarization position angles created by grains trapped on the draped ISMF may account for the higher significance fits to the downfield stars than for the upfield stars. This scenario awaits detailed modeling of grain alignment and opacity for grains in heliosheath regions.

5.2. Magnetic Filaments and Arcs

Figure 2 shows many polarization position angles organized into filamentary patterns that suggest a magnetic structure in the sky. Three filamentary structures echo the geometry of the heliosphere: Filament A (Section 5.2.1), and two magnetic arcs located around the port and starboard sides of the heliotail (Section 5.2.2). The geometric similarities between the filamentary structures and the heliosphere suggest that interstellar grains interacting with solar wind plasma in the outer heliosphere or heliosheath (Slavin et al. 2012, S12) also polarize background starlight sampled by the polarization data.

A deficit of low-mass ISDGs inside the heliosphere ($\ll 10^{16}$ g) has been inferred from comparing the measured grain mass distribution and the benchmark (Mathis et al. 1977) interstellar extinction curve (F99; Slavin et al. 2012; Krueger et al. 2015; Sterken et al. 2015). These low-mass interstellar grains are excluded from the heliosphere by high charge-to-mass ratios. The grains couple to the ISMF in the heliosheath regions, and provide a possible explanation for the polarizing grains that trace the filaments and arcs echoing heliosphere geometry in Figure 2, left.

The magnetic arcs are circular around the downwind direction and overlap the downwind ENA lobes identified in IBEX data (Zirnstein et al. 2017). The $50°$ of Arc 1 may also sample dust deflected around the heliopause at ~ 200 au downstream, as demonstrated in Figure 1 of Slavin et al. (2012) and based on simulations using the same heliosphere model as in Schwadron et al. (2009). These arc centers are also close to the Cetus Arc direction, where an anomalous clustering of the heliocentric velocities of interstellar absorption components has been identified (Gry & Jenkins 2014).

5.2.1. Filament A and Inflowing Interstellar Dust Grains

Polarization data that trace the magnetic field configuration denoted as "Filament A" sample a magnetic arc formed by smoothly varying polarization across the sky over an angular interval of $\sim 360°$ (Figure 7). Polarizations assigned to Filament A are plotted in red in Figure 7 and identified with star names in Appendix C. Filament A is symmetric about the heliosphere nose and blends into Arc 1 and Arc 2 in the region containing the tail of the heliosphere.

Ulysses and Galileo data collected before 1996 provided the basis for evaluating the upwind direction of interstellar dust flowing into the inner heliosphere (F99). Grains with dimensions that polarize optical light (radius $\leqslant 0.1$ μm) make negligible contributions to the inner heliosphere dust fluxes measured by Ulysses (Landgraf 2006). A χ^2 fit to these data yielded an upwind direction for inflowing interstellar grains toward $259° \pm 20°$, $8° \pm 10°$ (Appendix B in F99). This location is within 1σ of the He° inflow direction.

Figure 8, left, shows the 1σ, 2σ, and 3σ contours for the inflow direction of interstellar grains measured by Ulysses and Galileo (based on Figure 9 in F99). The 1σ uncertainties for the upwind dust flow direction are $259° \pm 20°$, $8° \pm 10°$. Figure 8, right, shows that Filament A overlaps the dust upwind direction, represented by a green bar. The overlap suggests that Filament A is formed by the interstellar grains filtered in heliosheath regions and excluded from the heliosphere by large charge-to-mass ratios.

Exclusion of dust grains from the heliosphere varies with the solar cycle as the Sun moves through the surrounding cloud at

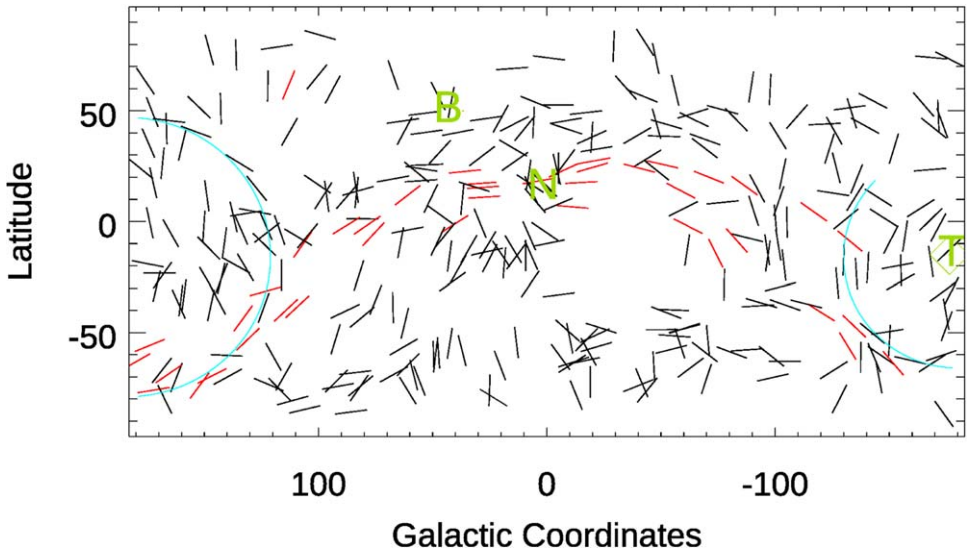

Figure 7. Polarization position angles of stars tracing the extended arc of polarization position angles that includes Filament A are plotted in red. The magnetic field traced by Filament A extends through the nose region of the heliosphere ("N") and appears to be displaced in the heliotail region that is within the two cyan-colored lunes, Arc 1 and Arc 2. The Hipparcos numbers of the stars forming the extended Filament are listed in Appendix C.

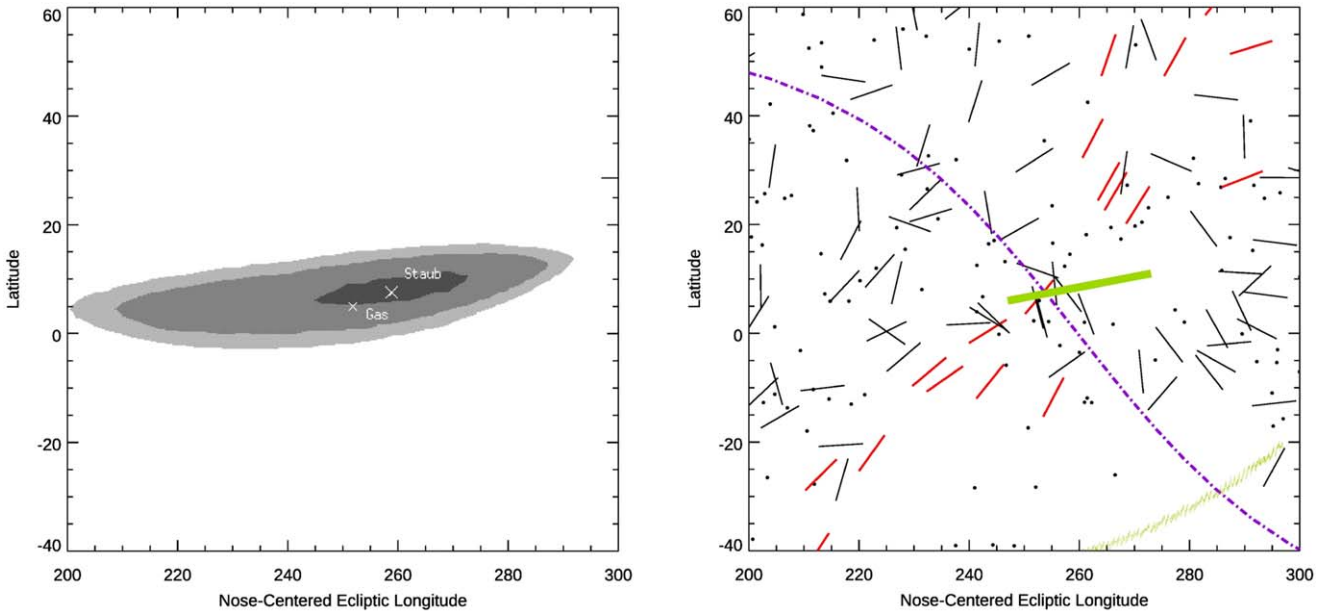

Figure 8. Left: the probability distribution for the upwind direction of the interstellar dust ("staub") grains flowing into the heliosphere based on Ulysses and Galileo data (Appendix 9 in F99 and M. Landgraf 2022, private communication). The 1σ, 2σ, and 3σ contours of the best-fit upwind dust direction are indicated in dark, medium, and light gray. The minimum χ^2 value ("x") is located at $\lambda, \beta = 259°, 8°$. Right: polarization position angles are plotted in ecliptic coordinates for stars in a region around the heliosphere nose, with position angles of stars tracing Filament A shown in red and dots identifying data where $P/\Delta P < 1.95$. The dotted line is the B–V plane. The green bar shows the axis of the 1σ uncertainty contour for the upwind direction of interstellar dust measured inside heliosphere. Note longitudes increase from right to left.

~5 au per year. A search for temporal variations in polarizations of Filament A stars may constrain models of its origin and also provide a ground-based diagnostic of the upwind outer heliosheath.

5.2.2. Magnetic Arcs around the Heliotail

The heliosphere distorts the ISMF lines during our journey through space. A pair of large magnetic arcs appear when polarization position angles are plotted in Galactic coordinates (Figure 2, left, cyan arcs). These features, denoted Arc 1 and Arc 2, are fragments of circles defined by centers and radii of ℓ, b, radius = 184°, −16°, 63° (Arc 1) and ℓ, b, radius = 180°, −16°, 50° (Arc 2). Arc 1 and Arc 2 have centers that are, respectively, 180° and 176° away from the direction of the heliosphere nose. The arcs are centered on the heliotail. These arcs echo features found in simulations of interstellar dust interacting with the heliosphere based on the propagation of idealized compact spherical silicate dust grains through a 3D MHD heliosphere (S12).

The centers of Arc 1 and Arc 2 also overlap the region of the sky where Gry & Jenkins (2014) identified a group of

interstellar absorption features (the "Cetus arc") that deviated from their kinematical model of the bulk flow of very local interstellar gas past the heliosphere. The axis of deformation, calculated from heliocentric velocities, is toward $\ell = 174.^{\circ}17 \pm 5.^{\circ}25$, $b = -12.^{\circ}10 \pm 4.^{\circ}21$ and overlaps the heliotail. Gry and Jenkins model the Cetus arc as shocked interstellar gas.

5.3. Outer Heliosheath

The complementary measurements of inflowing large grains and the excluded grains forming Filament A provide an unusual perspective on the grain population interacting with the heliosphere. The related geometry of Filament A, the 1.7 keV IBEX ribbon, Voyager kHz events, QSO scattering screens, and CMB multipole moments (Figure 9) suggests that all features trace an outer heliosphere region that is dominated by the ISMF shaping the heliosphere.

5.3.1. Voyager Kilohertz and Magnetometer Data

Remarkably, the Voyager spacecraft are traversing the regions where Filament A appears to form. Figure 2 shows that Filament A overlaps the 3 kHz emissions detected by Voyagers 1 and 2 (Kurth & Gurnett 2003). The emissions were detected during the years 1992–1994, when the two Voyager missions were inside the heliopause. The emissions were spread over an angle of 124°, and found by triangulation to be at distances from 120 to 139 au for the primary distance solution.

The magnetometers on board Voyager 1 and Voyager 2 provide measurements that constrain the morphology of the ISMF interacting with the heliosphere. The Filament A dust grains may be captured by the magnetic field in this region. Voyager 2 crossed the heliopause in the south on 2018 November 5 at 119.0 au, at ecliptic coordinates $\lambda = 119.^{\circ}0$, $\beta = -31.^{\circ}2$ ($\ell = 228.^{\circ}4$, $b = 5.^{\circ}2$) and found a smooth magnetic field that did not vary in direction (Burlaga et al. 2019, 2020). This is as expected for a magnetic flux tube draped over the heliosphere (Gurnett et al. 2021). The location where V2 crossed the heliopause is 95° from the ISMF direction $B_{\rm magpol}$. The near perpendicularity of the V2 trajectory and the direction of $B_{\rm magpol}$ are consistent with the hypothesis that $B_{\rm magpol} < 0$ star sightlines correspond to smoother regions of the ISMF interacting with the heliosphere.

5.3.2. Scattering Screens in QSO Sightlines

Narrow radio beams of compact QSO radio sources scintillate in turbulent foreground plasma that scatters the signal (Dennett-Thorpe & de Bruyn 2000; Lovell et al. 2008). Three twinkling QSOs overlap Filament A, J1819+3845 (ℓ, $b = 66°$, $b = 23°$; Dennett-Thorpe & de Bruyn 2000), PKS 1257-326 ($\ell = 305°$, $b = 30°$; Bignall et al. 2003), and PKS B1519-273 ($\ell = 340°$, $b = 24°$; Jauncey et al. 2003). These quasars show transient variability with annual cycles that could be explained by changes in the scattering screen or its orientation, implying the ISM is inhomogeneous at au scales (Bignall et al. 2003).

These QSOs may sample unstable plasma trapped on the ordered magnetic field upstream of the heliopause. QSO J1819 +3845 exhibits 30% variations on timescales of 30 minutes, indicating turbulence from compact overdense electron-scattering structures where $n(e) \sim 10$–10^3 cm^{-3} and a distance less than 3 pc (Vedantham et al. 2017). Such rapid variability, annual cycles in the characteristic timescale, and time delay in the variability pattern at different frequencies imply scintillation due the local plasma screen at distances less than a few

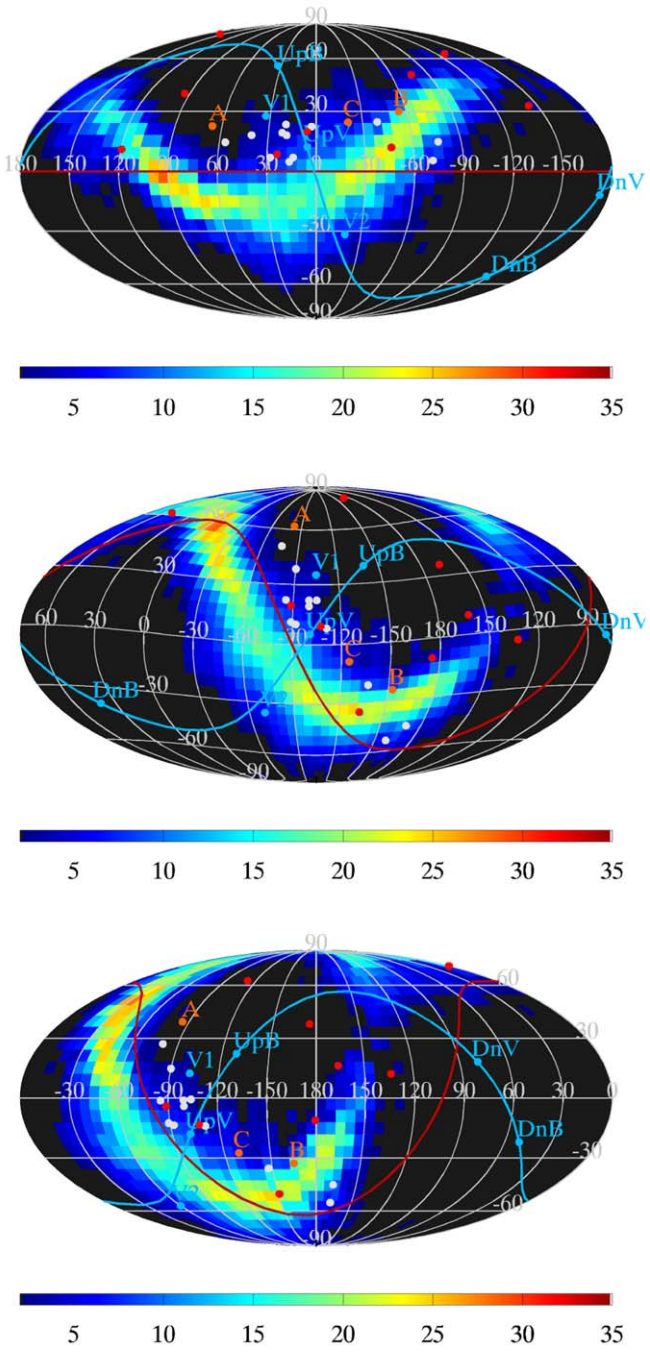

Figure 9. The IBEX ribbon is shown in Galactic (top), ecliptic (middle), and celestial (bottom) coordinates for the 9 yr maps of 1.7 keV ribbon ENAs (Schwadron et al. 2018). Locations of Voyager 1 and Voyager 2 are shown with cyan-colored letters and dots. Positions of the 3 kHz emissions detected by Voyager 1 and Voyager 2 are shown as white dots. Locations of three QSO intraday variables are identified with red letters A (J1819+3845), B (PKS 1257-326), and C (PKS B1519-273). The cyan-colored "V" letters indicate the current locations of Voyager 1 and Voyager 2. The direction and opposite directions of the local interstellar magnetic field are indicated by the cyan-colored "UpB" and "DnB." The upwind and downwind directions of the interstellar wind flowing the heliosphere are indicated by the cyan-colored "UpV" and "DnV." Red dots show the cosmic microwave background multiple moments found by Copi et al. (2007) in the WMAP ILC3 map.

parsecs. The elongated scattering feature traced by QSO J1819 +3845 appears to extend parallel to the ISMF (Figure 2 of Vedantham et al. 2017). That QSO scattering screens may trace the configuration of the ISMF interacting with the heliosphere is unexpected.

5.3.3. Echoes of the Local Interstellar Magnetic Field in the Cosmic Microwave Background

The CMB quadrupole and octopole components in WMAP data were shown to echo the heliosphere configuration (Copi et al. 2007). Comparisons of these CMB components and Voyager 3 kHz emissions indicated these features were spatially aligned (Frisch 2007). The great circle that bifurcates the CMB dipole moment passes within 5° of the heliosphere nose (Frisch 2010).

Of the nine CMB multipole components listed in Table 1 of Copi et al. (2007), the multipole components located at Galactic coordinates $\ell, b = (5\overset{\circ}{.}9, 19\overset{\circ}{.}6)$, $(23\overset{\circ}{.}9, 8\overset{\circ}{.}3)$, $(-46\overset{\circ}{.}3, 11\overset{\circ}{.}7)$, and $(-76\overset{\circ}{.}1, 50\overset{\circ}{.}0)$ overlap polarization data that trace the ISMF direction of Filament A. This supports the view that interstellar dust entrained in the ISMF interacting with the heliosphere provides a measurable foreground to the CMB. The full set of multiple moments reported by Copi et al. (2007) trace the configuration of the IBEX ribbon through a wider angle than obtained from the 3 kHz data (Figure 9).

5.3.4. The IBEX Ribbon

Figure 9 shows that the locations of three QSO intraday variables and the Voyager kilohertz emissions overlay Filament A, suggesting all phenomena arise in the outer heliosheath. These data are plotted together with the 1.7 keV IBEX ribbon in Galactic, ecliptic, and celestial coordinates. The ribbon data are from the 9 yr maps of 1.7 keV ENAs (Schwadron et al. 2018). The ∼30° offset of the 3 kHz emissions and QSO intraday variables from the ribbon toward the starboard side of the heliosphere (ecliptic west) is toward the upfield direction of the local ISMF.

Measurements of the parallax of the IBEX ribbon from opposite locations in the IBEX orbit during the first five years of IBEX data gave a ribbon distance of 140^{+84}_{-38} au (Swaczyna et al. 2016). This range overlaps the 113–139 au region of the Voyager 3 kHz emissions measured over a decade earlier (1992–1994, KG02), although uncertainties are large.

6. Summary

A large data set of the linear polarizations of stars within 40 pc is used to investigate the relationship between the ISMF shaping the heliosphere and the ambient ISMF. The primary findings are as follows.

1. The interstellar polarization data trace the ISMF shaping the heliosphere and the IBEX ribbon. The best-fitting ISMF direction is obtained from a statistical analysis of polarization position angles. Three data ensembles were tested for the best-fitting ISMF direction. The subset of stars located over 90° from the ISMF ("downfield" stars) found from fits to all-sky data provided the most significant ISMF direction.
2. The polarization data provide evidence for a magnetic shock front aligned with the boundaries between adjacent clouds in the downfield direction. The relative velocities of the colliding clouds may be super-Alfvénic.
3. A dark spot in the CMB is consistent with a viewpoint parallel to the ISMF that samples magnetic turbulence and the opaque axis of aligned grains.
4. Magnetic filaments and arcs are found throughout the sky. "Filament A" is shown to be a large-scale feature that is traced by polarization position angles that extend ∼300° around the heliosphere.
5. Filament A overlaps the 3 kHz radio emissions detected upstream of the heliopause by the Voyager spacecraft as well as the compact scattering screens in front of three distant QSOs. It also aligns with multipole components characterizing the CMB.
6. These common alignments suggest the presence of a magnetic flux tube in the outer heliosheath in which instabilities may cause dense plasma pockets.
7. Filament A appears where the smaller dust grains entrapped on the magnetic field lines would be deflected around the heliosphere, in contrast to the larger dust grains measured in situ by Ulysses and Galileo.
8. The coincidences between the CMB multipole moments, the aligned dust grains forming Filament A, and the IBEX ribbon suggests that the interstellar dust entrained in the ISMF interacting with the heliosphere may provide a measurable foreground to the CMB.

This work was supported in part by the Interstellar Boundary Explorer (IBEX) mission as a part of the NASA Explorer program (80NSSC20K0719), and the Interstellar Mapping and Acceleration Probe (IMAP) mission as a part of the NASA Solar Terrestrial Probes program (80GSFC19C0027). We are grateful to the Institute for Astronomy, University of Hawaii, for the observing time allocated for us on the UH88 and T60 telescopes, and to the University of Tasmania (UTAS) for the observing time at the H127 telescope, Greenhill Observatory, supported in part by the University of Tasmania Foundation. The H127 telescope is funded in part by grant No. LE110100055 from the Australian Research Council. This research is based in part on observations made with the Nordic Optical Telescope (NOT), owned in collaboration by the University of Turku and Aarhus University, and operated jointly by Aarhus University, the University of Turku and the University of Oslo, representing Denmark, Finland and Norway, the University of Iceland and Stockholm University at the Observatorio del Roque de los Muchachos, La Palma, Spain, of the Instituto de Astrofisica de Canarias. We acknowledge support from the Magnus Ehrnrooth foundation, and ERC Advanced Grant Hot-Mol ERC-2011-AdG-291659. M.B. was supported by the Polish National Science Center grant No. 2019-35-B-ST9-01241. P.C.F. acknowledges funding from NASA IBEX and IMAP missions and HST-GO-14084. A.M. M.'s research and his collection of optical polarimetry at IAG-USP have been supported over the years by multiple grants from the São Paulo state funding agency FAPESP and from the Brazilian agency CNP.

Appendix A
Spacemarks and the *B–V* Plane

Spacemarks in the sky that are relevant to the local ISMF configuration include the heliosphere nose and tail. The tail has a nominal direction 180° from the nose, although predictions

by heliosphere models vary (e.g., Pogorelov et al. 2008; Opher et al. 2017), A spacemark that determines a symmetry of the heliosphere is the *B–V* plane that divides the sky into two hemispheres. Magnetic hemispheres are divided into regions within 90° ($B_{\rm magpol} < 0$) or more than 90° ($B_{\rm magpol} > 0$) of $B_{\rm magpol}$ (Section 3).

The IBEX-Lo detector yields precise data on the Sun's motion through the surrounding interstellar gas (Fuselier et al. 2009). The measurement technique (Möbius et al. 2009) and analysis methodology yield the flow direction of interstellar He° (Swaczyna et al. 2015, Appendix A). Analysis of the inflow of interstellar neutral He at 1 au gives an upwind direction toward ecliptic coordinates $\lambda = 255.^{\circ}8 \pm 0.^{\circ}5$, $\beta = 5.^{\circ}16 \pm 0.^{\circ}10$, velocity $= 25.8 \pm 0.4$ km s^{-1}, and temperature 7439 ± 260 K (Bzowski et al. 2015).

The direction of the unperturbed interstellar B-field was obtained by fitting the position and radius of the IBEX ribbon of enhanced emission of energetic neutral atoms (Zirnstein et al. 2016). The ribbon was unexpectedly discovered by IBEX (Funsten et al. 2009; McComas et al. 2009) and shown to correspond to the locus of points upstream of the heliosphere where the ISMF is perpendicular to the sightline in 3D global heliosphere models (Schwadron et al. 2009). The ribbon is formed by secondary ENA emission upstream of the heliosphere. The ENAs result from neutralization by charge exchange of 1 keV protons, which perform Lorentzian gyromotion around the field lines of interstellar magnetic *B* field distorted by the heliosphere (Heerikhuisen et al. 2010).

The relation between the ribbon, the ISMF, and the orientation of the *B–V* plane was also established indirectly by in situ sampling of interstellar neutral atoms by IBEX-Lo. In the absence of the interstellar and solar magnetic fields, the heliosphere is expected to be axially symmetric around an axis parallel to the direction of the solar motion relative to the surrounding interstellar matter. A magnetic field of about 3 μG in the local interstellar matter results in a deformation of the heliosphere, yielding a non-axially-symmetric flow of interstellar matter through the heliopause. MHD-kinetic simulations of the heliosphere reproduce these asymmetries (Izmodenov & Baranov 2006; Pogorelov & Zank 2006; Pogorelov et al. 2009; Izmodenov & Alexashov 2015).

Interactions between the charged and neutral components of interstellar gas result in the formation of a secondary population of interstellar neutral H and He atoms (Bzowski et al. 2017). The trajectories of these secondaries trace the distortion of the heliosphere, with a preferential flow direction along the *B–V* plane (Kubiak et al. 2019). Kubiak et al. (2016) determined the direction of inflow of secondary He, calculated the orientation of the *B–V* plane, and showed that it agreed with the orientation based on the ribbon. It also agrees with the *B–V* plane based on the interstellar neutral H (Lallement et al. 2005). The filtration of charged ISDGs interacting with the heliosphere has been modeled in several detailed studies (Frisch et al. 1999; Linde & Gombosi 2000; Czechowski & Mann 2003; Slavin et al. 2012; Sterken et al. 2012; Alexashov et al. 2016).

Appendix B
Notes on Intrinsic Polarizations

The polarization measured from any star is a combination of interstellar and possible intrinsic polarizations. We are interested only in the interstellar component, so efforts have been made to exclude intrinsically polarized stars.

Interstellar polarizations are expected to be weak for stars within 40 pc, where typically $N(\mathrm{H}^{\circ}) < 10^{18.5}$ cm^{-2}. Additional dust may be associated with ionized gas. Standard relations between polarization strength, color excess $E(B-V)$, and $N(\mathrm{H}^{\circ})$ are consistent with observed polarization strengths once ionized gas is included (F15a).

Recent work gives an indication of the typical levels of local interstellar polarization. Working with a small set of stars, mostly within 30 pc, Cotton et al. (2017) estimated ratios of interstellar polarization strength of 0.26 ppm pc^{-1} above 30 deg Galactic latitude (Bailey et al. 2010). At more southerly latitudes values of ~0.8 ppm pc^{-1} within 14.5 pc and ~1.64 ppm pc^{-1} beyond 14.5 pc have been found. Working with a star sample that included both northern and southern hemisphere stars, Piirola et al. (2020) find a dependence of maximum polarization on distance of 2.9 ppm pc^{-1}. Consequently, even small intrinsic polarizations could dominate for an individual star. In this study the expectation is that position angles of intrinsic polarizations will trace randomly oriented magnetic field directions that will not bias the best-fitting ISMF for large subsets of the ISMF data.

Nearby space is devoid of stars that might show the largest intrinsic polarizations, such as B-type stars, rapid rotators, or magnetic types (Cotton et al. 2017; Wade et al. 2000). Rapid rotation may also produce small polarizations (Bailey et al. 2020). In practice there are few B-type stars within 40 pc.

The influence of the most extreme polarized stars is minimized by the condition $P/\Delta P < 6$, but this still leaves a number of smaller effects. Stars from (Piirola et al. 2020) that are utilized in this study (over half of the data set) were screened to exclude possible intrinsic polarizations, and astrometric distances were required to match the photometric distances. Active stars and those with unusual spectral types and known intrinsically polarized stars were avoided.

The data set predominantly consists of ordinary main-sequence stars. In general, spectral types likely to be intrinsically polarized are not included in the star sample, nor are stars at the other end of the Hertzsprung–Russell diagram, which might display polarization due to inherent dust production or irregularly shaped photospheres (Serkowski 1966; Kemp et al. 1986; Cotton et al. 2020a).

Reflection effects in close binaries can have quite large polarizations, but also small ones depending on their separation, spectral types, and other factors (Bailey et al. 2019; Cotton et al. 2020b). Hot Jupiter-like exoplanets may also have small polarizations, 20 ppm or less, through a similar mechanism (Seager et al. 2000). Extensive debris disks such as in systems like Beta Pic, AU Mic, or HD 172555 (Gledhill et al. 1991; Graham et al. 2007; Marshall et al. 2020) may also result in several 10s of ppm polarization, though in most disk systems the fractional polarization is smaller (e.g., Vandeportal et al. 2019).

Appendix C
Filament A Stars

Polarizations forming "Filament A" (Section 5.2.1) appear to sample a large-scale magnetic field line traced by polarization position angles that vary continuously over an arc of nearly 360°. The stars plotted in red in Figure 7 show the approximate configuration of the arc denoted "Filament A" here. The

Hipparcos numbers of the stars plotted in red in Figure 7 are as follows: HIP 400, 1813, 4103, 4290, 5534, 6405, 6456, 6537, 6779, 7446, 8497, 11029, 12048, 12837, 16012, 19095, 21861, 32349, 39757, 44143, 45238, 50888, 57021, 59072, 61923, 61932, 65109, 65378, 68932, 68933, 68939, 69165, 74500, 75363, 78330, 78843, 79165, 82283, 82396, 84068, 86032, 86742, 87108, 88324, 88923, 89912, 90165, 91262, 93185, 94068, 99026, 101875, 102488, 104587, 112812, 114570, 114570, and 900121. Data sources for these stars are summarized in Section 2.1. Stars with polarization position angles listed as sampling Filament A have been selected visually based on position angles that trace an arc in the sky. A more rigorous definition of the filament configurations requires numerical analysis beyond the scope of this paper.

ORCID iDs

P. C. Frisch https://orcid.org/0000-0001-6538-4015
V. Piirola https://orcid.org/0000-0003-0186-206X
A. B. Berdyugin https://orcid.org/0000-0002-9353-5164
C. Heiles https://orcid.org/0000-0002-7456-8067
A. Cole https://orcid.org/0000-0003-0303-3855
S. J. Wiktorowicz https://orcid.org/0000-0003-4483-5037
D. V. Cotton https://orcid.org/0000-0003-0340-7773
L. Kedziora-Chudczer https://orcid.org/0000-0001-7212-0835
N. A. Schwadron https://orcid.org/0000-0002-3737-9283
M. Bzowski https://orcid.org/0000-0003-3957-2359
D. J. McComas https://orcid.org/0000-0001-6160-1158
E. J. Zirnstein https://orcid.org/0000-0001-7240-0618
H. O. Funsten https://orcid.org/0000-0002-6817-1039
Seth Redfield https://orcid.org/0000-0003-3786-3486

References

Adams, T. F., & Frisch, P. C. 1977, ApJ, 212, 300
Alexashov, D. B., Katushkina, O. A., Izmodenov, V. V., & Akaev, P. S. 2016, MNRAS, 458, 2553
Andersson, B.-G., Lazarian, A., & Vaillancourt, J. E. 2015, ARA&A, 53, 501
Appenzeller, I. 1968, ApJ, 151, 907
Bailey, J., Bott, K., Cotton, D. V., et al. 2021, MNRAS, 502, 2331
Bailey, J., Cotton, D. V., Howarth, I. D., Lewis, F., & Kedziora-Chudczer, L. 2020, MNRAS, 494, 2254
Bailey, J., Cotton, D. V., & Kedziora-Chudczer, L. 2017, MNRAS, 465, 1601
Bailey, J., Cotton, D. V., Kedziora-Chudczer, L., De Horta, A., & Maybour, D. 2019, NatAs, 3, 636
Bailey, J., Kedziora-Chudczer, L., Cotton, D. V., et al. 2015, MNRAS, 449, 3064
Bailey, J., Lucas, P. W., & Hough, J. H. 2010, MNRAS, 405, 2570
Berdyugin, A., Piirola, V., & Teerikorpi, P. 2014, A&A, 561, A24
Bignall, H. E., Jauncey, D. L., Lovell, J. E. J., et al. 2003, ApJ, 585, 653
Bohlin, R. C., Savage, B. D., & Drake, J. F. 1978, ApJ, 224, 132
Burlaga, L. F., Ness, N. F., Berdichevsky, D. B., et al. 2019, ApJ, 877, 31
Burlaga, L. F., Ness, N. F., Berdichevsky, D. B., et al. 2020, ApJL, 901, L2
Bzowski, M., Czechowski, A., Frisch, P. C., et al. 2019, ApJ, 882, 60
Bzowski, M., Kubiak, M. A., Czechowski, A., & Grygorczuk, J. 2017, ApJ, 845, 15
Bzowski, M., Swaczyna, P., Kubiak, M. A., et al. 2015, ApJS, 220, 28
Copi, C. J., Huterer, D., Schwarz, D. J., & Starkman, G. D. 2007, PhRvD, 75, 023507
Cotton, D. V., Bailey, J., De Horta, A. Y., Norris, B. R. M., & Lomax, J. R. 2020a, RNAAS, 4, 39
Cotton, D. V., Bailey, J., Kedziora-Chudczer, L., & De Horta, A. 2020b, MNRAS, 497, 2175
Cotton, D. V., Bailey, J., Kedziora-Chudczer, L., et al. 2016, MNRAS, 455, 1607
Cotton, D. V., Marshall, J. P., Bailey, J., et al. 2017, MNRAS, 467, 873
Cotton, D. V., Marshall, J. P., Frisch, P. C., et al. 2019, MNRAS, 483, 3636
Czechowski, A., & Mann, I. 2003, JGRA, 108, 13
Dennett-Thorpe, J., & de Bruyn, A. G. 2000, ApJL, 529, L65
Frisch, P., & Dwarkadas, V. V. 2018, arXiv:1801.06223
Frisch, P. C. 1994, Sci, 265, 1423
Frisch, P. C. 1996, SSRv, 78, 213
Frisch, P. C. 2007, arXiv:0707.2970
Frisch, P. C. 2010, ApJ, 714, 1679
Frisch, P. C., Andersson, B.-G., Berdyugin, A., et al. 2015a, ApJ, 805, 60
Frisch, P. C., Berdyugin, A., Piirola, V., et al. 2015b, ApJ, 814, 112
Frisch, P. C., Berdyugin, A. B., Piirola, V., et al. 2018, arXiv:1806.02806
Frisch, P. C., Dorschner, J. M., Geiss, J., et al. 1999, ApJ, 525, 492
Frisch, P. C., Grodnicki, L., & Welty, D. E. 2002, ApJ, 574, 834
Frisch, P. C., Redfield, S., & Slavin, J. 2011, ARA&A, 49, 237
Frisch, P. C., & Schwadron, N. A. 2014, in ASP Conf. Ser. 484, Outstanding Problems in Heliophysics: From Coronal Heating to the Edge of the Heliosphere, ed. Q. Hu & G. P. Zank (San Francisco, CA: ASP), 42
Funsten, H. O., Allegrini, F., Crew, G. B., et al. 2009, Sci, 326, 964
Funsten, H. O., DeMajistre, R., Frisch, P. C., et al. 2013, ApJ, 776, 30
Fuselier, S. A., Allegrini, F., Funsten, H. O., et al. 2009, Sci, 326, 962
Gledhill, T. M., Scarrott, S. M., & Wolstencroft, R. D. 1991, MNRAS, 252, 50P
Graham, J. R., Kalas, P. G., & Matthews, B. C. 2007, ApJ, 654, 595
Gry, C., & Jenkins, E. B. 2014, arXiv:1404.0326
Grzedzielski, S., & Lallement, R. 1996, SSRv, 78, 247
Gurnett, D. A., Kurth, W. S., Stone, E. C., et al. 2021, AJ, 161, 11
Hanson, A. J., Fu, C.-W., & Frisch, P. C. 2003, Constraint-Based Astronometric Modeling Tools (Berlin: Springer), 437
Heerikhuisen, J., Pogorelov, N. V., Zank, G. P., et al. 2010, ApJL, 708, L126
Heiles, C. 1998, in IAU Coll. 166: The Local Bubble and Beyond, ed. D. Breitschwerdt, M. J. Freyberg, & J. Truemper (Berlin: Springer), 229
Heiles, C. 2000, AJ, 119, 923
Izmodenov, V. V., & Alexashov, D. B. 2015, ApJS, 220, 32
Izmodenov, V. V., & Baranov, V. B. 2006, ISSIR, 5, 67
Jauncey, D. L., Johnston, H. M., Bignall, H. E., et al. 2003, Ap&SS, 288, 63
Kemp, J. C., Henson, G. D., Kraus, D. J., et al. 1986, ApJL, 301, L35
Krueger, H., Strub, P., Sterken, V. J., & Grün, E. 2015, ApJ, 812, 139
Kubiak, M. A., Bzowski, M., & Sokół, J. M. 2019, ApJ, 882, 114
Kubiak, M. A., Swaczyna, P., Bzowski, M., et al. 2016, ApJS, 223, 25
Kurth, W. S., & Gurnett, D. A. 2003, JGRA, 108, 8027
Lallement, R., Quémerais, E., Bertaux, J. L., et al. 2005, Sci, 307, 1447
Landgraf, M. 2006, in Solar Journey: The Significance of Our Galactic Environment for the Heliosphere and Earth, ed. P. C. Frisch (Berlin: Springer), 195
Lazarian, A., & Hoang, T. 2019, ApJ, 883, 122
Lehner, N., Jenkins, E., Gry, C., et al. 2003, ApJ, 595, 858
Leroy, J. L. 1993, A&AS, 101, 551
Linde, T. J., & Gombosi, T. I. 2000, JGR, 105, 10411
Linsky, J. L., Rickett, B. J., & Redfield, S. 2008, ApJ, 675, 413
Lovell, J. E. J., Rickett, B. J., Macquart, J. P., et al. 2008, ApJ, 689, 108
Marshall, J. P., Cotton, D. V., Bott, K., et al. 2016, ApJ, 825, 124
Marshall, J. P., Cotton, D. V., Scicluna, P., et al. 2020, MNRAS, 499, 5915
Mathewson, D. S., & Ford, V. L. 1970, MmRAS, 74, 139
Mathis, J. S., Rumpl, W., & Nordsieck, K. H. 1977, ApJ, 217, 425
McComas, D. J., Allegrini, F., Bochsler, P., et al. 2009, Sci, 326, 959
Möbius, E., Bochsler, P., Bzowski, M., et al. 2009, Sci, 326, 969
Opher, M., Drake, J. F., Swisdak, M., Zieger, B., & Toth, G. 2017, ApJL, 839, L12
Panopoulou, G. V., Dickinson, C., Readhead, A. C. S., Pearson, T. J., & Peel, M. W. 2021, ApJ, 922, 210
Perryman, M. A. C. 1997, A&A, 323, L49
Piirola, V. 1977, A&AS, 30, 213
Piirola, V., Berdyugin, A., Frisch, P. C., et al. 2020, A&A, 635, A46
Pogorelov, N. V., Heerikhuisen, J., Mitchell, J. J., Cairns, I. H., & Zank, G. P. 2009, ApJL, 695, L31
Pogorelov, N. V., Heerikhuisen, J., & Zank, G. P. 2008, ApJL, 675, L41
Pogorelov, N. V., & Zank, G. P. 2006, in ASP Conf. Ser. 359, Numerical Modeling of Space Plasma Flows, ed. G. P. Zank & N. V. Pogorelov (San Francisco, CA: ASP), 184
Redfield, S., & Linsky, J. L. 2008, ApJ, 673, 283
Rogerson, J. B., York, D. G., Drake, J. F., et al. 1973, ApJL, 181, L110
Santos, F. P., Corradi, W., & Reis, W. 2011, ApJ, 728, 104
Schwadron, N. A., Allegrini, F., Bzowski, M., et al. 2018, ApJS, 239, 1
Schwadron, N. A., Bzowski, M., Crew, G. B., et al. 2009, Sci, 326, 966

Schwadron, N. A., & McComas, D. J. 2021, ApJ, 914, 129
Schwadron, N. A., Moebius, E., Leonard, T., et al. 2015a, ApJS, 220, 25
Schwadron, N. A., Richardson, J. D., Burlaga, L. F., McComas, D. J., & Moebius, E. 2015b, ApJL, 813, L20
Schwarz, D. J., Copi, C. J., Huterer, D., & Starkman, G. D. 2016, CQGra, 33, 184001
Seager, S., Whitney, B. A., & Sasselov, D. D. 2000, ApJ, 540, 504
Serkowski, K. 1966, IBVS, 141, 1
Slavin, J. D., & Frisch, P. C. 2008, A&A, 491, 53
Slavin, J. D., Frisch, P. C., Müller, H.-R., et al. 2012, ApJ, 760, 46
Sterken, V. J., Altobelli, N., Kempf, S., et al. 2012, A&A, 538, A102
Sterken, V. J., Strub, P., Krüger, H., von Steiger, R., & Frisch, P. 2015, ApJ, 812, 141
Swaczyna, P., Bzowski, M., Christian, E. R., et al. 2016, ApJ, 823, 119
Swaczyna, P., Bzowski, M., Kubiak, M. A., et al. 2015, ApJS, 220, 26
Tinbergen, J. 1982, A&A, 105, 53
Van Leeuwen, F. 2008, yCat, 1311, 0
Vandeportal, J., Bastien, P., Simon, A., Augereau, J.-C., & Storer, É. 2019, MNRAS, 483, 3510
Vedantham, H. K., de Bruyn, A. G., & Macquart, J. 2017, ApJL, 849, L3
Wade, G. A., Donati, J. F., Landstreet, J. D., & Shorlin, S. L. S. 2000, MNRAS, 313, 851
Wiktorowicz, S. J., & Nofi, L. A. 2015, ApJL, 800, L1
Wolleben, M. 2007, ApJ, 664, 349
Zirnstein, E. J., Heerikhuisen, J., Funsten, H. O., et al. 2016, ApJL, 818, L18
Zirnstein, E. J., Heerikhuisen, J., Zank, G. P., et al. 2017, ApJ, 836, 238